

Microstructure and microchemistry of flash sintered $K_{0.5}Na_{0.5}NbO_3$

Gulean CORAPCIOGLU,[†] Mehmet Ali GULGUN, Kim KISSLINGER,^{*}

Saso STURM,^{**} Shikhar.K. JHA^{***} and Rishi RAJ^{***}

Faculty of Engineering and Natural Sciences, Sabanci University, Tuzla, Istanbul, TURKEY

^{*}Center for Functional Nanomaterials, Brookhaven National Laboratory, Upton, New York, USA

^{**}Nanostructured Materials, Jozef Stefan Institute, Ljubljana, SLOVENIA

^{***}University of Colorado at Boulder, Department of Mechanical Engineering, Boulder, CO, USA

Flash sintering experiments were performed, for the first time, on sodium potassium niobate (KNN) ceramics. A theoretical density of 94% was achieved in 30 s under 250 V/cm electric-field at 990°C. These conditions are ~100°C lower and faster than the conventional sintering conditions. Grains tended to grow after 30 s. flash sintering duration under constant electric-field. Detailed microstructural and chemical investigations of the sample showed that there was inhomogenous Na, K distribution and it resembles a core-shell structure where K is more in the shell and Na is more in the core region. The inhomogenous distribution of Na and K was correlated with the doubling of the unit cell within the grain along 002 direction. Compositional equilibrium is achieved after a heat treatment at 1000°C for 4 h. The compositional variations appeared to have been linked to grain boundary melting during flash and consequent recrystallization as the sample cooled.

©2016 The Ceramic Society of Japan. All rights reserved.

Key-words : Flash sintering, TEM, STEM-EDX, Lead-free, Core-shell

[Received November 18, 2015; Accepted February 11, 2016]

1. Introduction

$K_{1-x}Na_xNbO_3$ abbreviated as KNN, is one of the most investigated lead-free ferroelectric systems after the environmental regulations which restricted the use of hazardous substances, like lead (Pb) in electrical and electronic equipment. KNN is the solid solution between ferroelectric $KNbO_3$ and anti-ferroelectric $NaNbO_3$. It has a perovskite (ABO_3) crystal structure and a high Curie temperature (420°C). The main problems associated with the poor sintering ability of KNN are the narrow range of sintering temperatures (melting temperature at about 1140°C, at $x = 0.5$), volatilization of alkali elements, and formation of secondary phases. In addition, irrespective of the starting morphology of the powders, KNN grains take on strong (100) faceted morphology during the thermal treatment. This morphological transition leaves behind gaps between differently oriented grains. These gaps coarsen as particle growth takes place.¹⁾⁻⁴⁾ Several methods have been used to promote densification; spark plasma sintering,⁵⁾ hot pressing,^{3),4)} addition of sintering additives such as Cu,⁶⁾ Li-Ta,^{4),7)} $K_{5.4}Cu_{1.3}Ta_{10}O_{29}$ (KCT).⁸⁾ Full densification was obtained only by spark plasma sintering (SPS) and hot-pressing (HP) which require high cost for mass production. Texturing was introduced as an effective way of enhancing electrical properties.⁹⁾

Flash sintering, an electric-field assisted sintering technique that was introduced by Raj's Group¹⁰⁾ at University of Colorado, is used for the first time, on sodium potassium niobate (KNN) ceramics. In flash sintering an electric-field is applied to the sample via two electrodes while the sample is heated. After

reaching a threshold temperature sintering occurs in a few seconds. Flash sintering is characterized by a non-linear increase in conductivity just after the onset of the flash. The higher the electric-field the lower the flash temperature. Power dissipation, I^2R , ($V=I^*R$) increases as the resistance falls under voltage control. The non-linear increase in the current in the specimen is controlled by setting a current limit at the beginning of the experiment. When the limit value is reached power supply switches to current control. After that, power dissipation, I^2R , reaches a quasi-steady-state rate depending on the reduction of the resistance leads to a stable specimen temperature.^{11),12)}

Flash sintering was applied to yttria,¹³⁾ yttria doped zirconia,¹⁰⁾ Mg doped alumina,¹⁴⁾ Co_2MnO_4 ,¹⁵⁾ SiC,¹⁶⁾ $SrTiO_3$ ¹⁷⁾ and TiO_2 ¹⁸⁾ up to now. It usually reduces the sintering temperature compared to conventional sintering and prevents grain growth. However for $SrTiO_3$ and TiO_2 at higher applied fields (150 V/cm) grain growth was observed.

Raj et al. proposed three possible mechanisms to explain the "flash" event. One of these mechanisms is (1) Joule heating, (an increase in temperature via electrical energy), at grain boundaries. It would increase both grain boundary diffusion and electrical conductivity through the boundaries. The effect of Joule heating was reported in yttria doped tetragonal zirconia (Y-TZP) and SiC. However, Raj et al. argued that the activation that are required for the fast sintering/diffusion rate observed during solid state sintering could not be achieved by Joule heating only. Therefore yet other mechanisms must be operative during flash sintering. Another proposed mechanism was (2) formation of Frenkel defect pairs and their ionization under the applied electric-field. It is known that the electrical conductivity is controlled by fast moving charged species whereas sintering is controlled by slow moving species. An abrupt increase in both electrical conductivity and solid-state diffusion during flash sintering was explained

[†] Corresponding author: G. Corapcioglu; E-mail: gulcanc@sabanciuniv.edu

[‡] Preface for this article: DOI <http://dx.doi.org/10.2109/jcersj2.124.P4-1>

by the formation and motion of the Frenkel defect pairs. The last possibility was (3) space charge layer adjacent to grain boundaries (can have strength of 10–1000 V cm⁻¹) interacting with external electric-field and changing the diffusion kinetics.^{10,11} Positive electric charge around grain boundaries were determined for Al₂O₃ by observing grain boundary motion under bias¹⁹ and visualized for Mn doped SrTiO₃ by electron holography.²⁰

Narayan suggested that ionic and electronic transport along dislocations and grain boundaries were increased depending on the increase in the defect segregation. As a result, dislocation mobility and selective Joule heating rose creating a selective melting of grain boundaries. Therefore, higher sintering rates observed during flash sintering was claimed to be due to 6–8 orders of magnitude higher diffusivities in the melted grain boundaries. These boundaries were devoid of any glassy film at the end of cooling.²¹

Zhang and co-workers claimed that flash initiated as a thermal runaway for ZnO based systems. They found ~320°C reduction on the flash sintering temperature of powder ZnO compared to single crystal ZnO (flash temperature for single crystal ~870°C and flash (sintering) temperature for powder ZnO ~550°C) and emphasized the importance of grain boundaries during flash.²²

In this study, flash sintering behavior of KNN ceramics was investigated. Microstructural and chemical characterization of flash sintered KNN emphasized how the flash sintered microstructure and chemistry were different from conventionally sintered KNN. The interpretation of the results shed light to the phenomena that was active during flash sintering process in these ceramics.

2. Experimental procedure

K_{0.5}Na_{0.5}NbO₃ powders were synthesized by conventional solid-state method. Calculated amounts of Na₂CO₃, K₂CO₃ and Nb₂O₅ were ball milled for 12 h in isopropanol environment with zirconia balls. Prior to mixing the powders in stoichiometric ratios were dried for 3 h at 200°C to remove the adsorbed water from these compounds. KNN powders were synthesized at 800°C for 2 h. After mixing the synthesized powders with binder, 2 wt % polyvinyl butyral (PVB), dog bone-shaped specimens were uniaxially pressed at 200 MPa. The gauge section of the dog bone was 20 mm × 3.5 mm × 1.2 mm. The green density of the sample was around 0.63. Samples were held at 550°C for 1 h. for binder burn out. Sintering experiments were conducted by applying a voltage to the specimen while the furnace temperature was increasing at a constant heating rate. **Figure 1** shows a schematic of flash sintering experimental set up. Two platinum electrodes were used both to suspend the dog bone shaped sample and to apply electric-field to the sample. Constant voltage was applied to the sample after 550°C while the temperature was increasing at a rate of 10°C/min. Sintering experiments were performed at 100–500 V/cm., 7–40 mA/mm², 10–60 s. in air atmosphere. Conventional sintering of pellets made up of the same powders was conducted at 1100°C for 2 h in air for comparison.

Shrinkage data were recorded by a CCD camera by taking photographs of the sample ten frame per second. Densities were both measured by Archimedes method and analyzed from SEM micrographs of the polished samples by UTHSCSA Image Tool Program (developed in the Department of Dental Diagnostic Science at The University of Texas Health Science Center, San Antonio, Texas).

Platinum paste was used to provide good electrical contact between sample and platinum wires and to form a uniform electric-field through the gauge section of the sample.

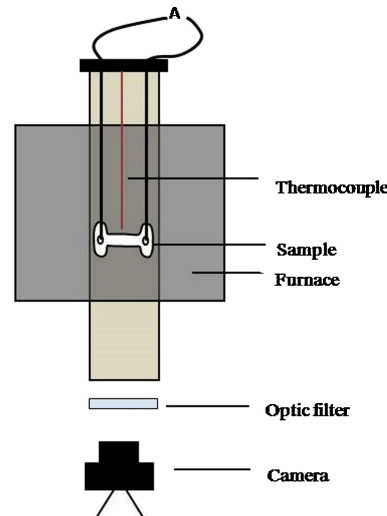


Fig. 1. The schematic of flash sintering set up.

Density of the sample was calculated by linear shrinkage data of the sample. Linear shrinkage strain was calculated with the equation $\varepsilon = \ln(L/L_0)$, where L_0 is initial length, L is time dependent gauge length, ρ_g is green density. Density is calculated with the equation $\rho = \rho_g e^{-3\varepsilon}$ where ε is linear shrinkage strain.

Specimen temperatures were estimated from Black- Body radiation model. Steady-state power density values were used to calculate the specimen temperature. According to the model, relation between the specimen temperature and furnace temperature is given by the formula:^{11,18}

$$\frac{T^*}{T_o} = \left[1 + \frac{1000Wv}{\sigma T_o^4} \left(\frac{V}{A} \right) \right]^{1/4} \quad (1)$$

where T_o is the furnace temperature (K), T^* is the specimen temperature (K), Wv is the power dissipation per unit volume of the specimen (mW/mm³), V/A is volume to surface area of the specimen and σ is the blackbody radiation constant equal to $5.67 \times 10^{-8} \text{ W}/(\text{m}^2\text{K}^4)$. Structural characterization was performed by using X-ray powder diffractometer, (Bruker AXS D8 Advance, Karlsruhe, Germany), by using Cu K α radiation. SEM micrographs and chemical analysis were done by SEM JEOL 6010 LV equipped by EDX detector. Polished (down to 1 μm by diamond paste) surfaces were examined by secondary electron mode. TEM sample was prepared by Focused Ion Beam (FIB) and was examined in a JEOL ARM200 ColdFEG, high-resolution, scanning transmission electron microscope (HR-STEM). Chemical composition was investigated by analytical electron microscopy utilizing a STEM equipped with an EDS spectrometer (JEOL Centurion EDX spectrometer).

3. Results

Sample was recorded with a CCD camera during the experiment. **Figure 2** shows the images of the sample taken during flash sintering. Picture number 1 resembles just before the flash, number 2: initiation of flash and number 3: during flash.

X-ray Diffraction analysis showed that both conventional sintered and flash sintered samples had a “single phase” KNN. There were no secondary ‘phases’ forming during flash sintering. Results of a constant heating rate experiment conducted at 250 V/cm and 20 mA/mm² are shown in **Fig. 3**. The flash sintering has two main regimes. The first part of the event spanned the time from the start of the experiment until the power spike was



Fig. 2. Images of the sample before the flash, initiation of flash and during flash sintering.

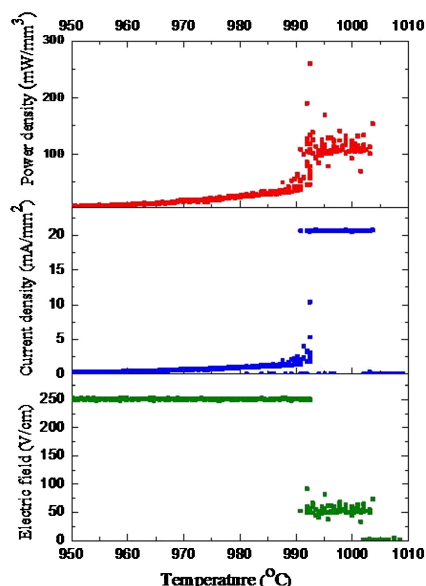


Fig. 3. Flash sintering cycle with applied field, current density, power density with respect to temperature.

observed. During this period the voltage was kept constant. This part is named voltage-control region. After the power spike, when the current limit of 20 mA/mm^2 was obtained, the current-control region commenced. During constant current region, electric-field and the power dissipation settled into a quasi-steady state value at about 50 V/cm and 109 mW/mm^3 , respectively. Power dissipated in the sample was calculated by multiplying applied voltage with the current. The sharp increase in the power was related to the sudden increase in the conductivity of the sample in the voltage-control region. When current limit was reached, the voltage in the specimen began to drop causing a decrease in power dissipation. After a short period, power dissipation tended towards a quasi-steady state as shown in Fig. 3 (current-control region). In this stage, the conductivity of the sample is higher as it is shown in the drop of the voltage value.

Constant heating rate experiments were conducted to investigate the flash sintering temperature at different electric-fields between $100\text{--}500 \text{ V/cm}$. The reported flash temperatures were taken as the temperature where steep increase in power density (i.e. in conductivity) was observed (Fig. 4).

As the applied electric-field increased both peak value of power dissipation and power dissipation at quasi-steady state (i.e. current control region) increased. Power densities for different field strengths at quasi-steady state are shown in Table 1. Specimen temperatures were calculated depending on the black body radiation model in Eq. (1). Sintering at lower electric-fields required high temperatures to flash. The (calculated) specimen temperatures for lower fields were very close to the melting point (1140°C) of the sample taken from the phase diagram.³⁾

Figure 5 shows the correlation between power density and

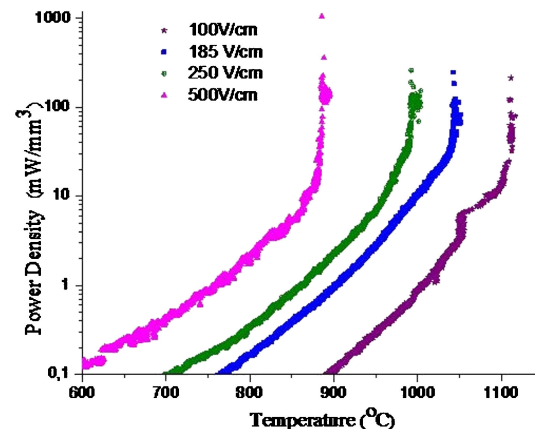


Fig. 4. Power densities for the samples with different electric-fields at 20 mA/mm^2 current density for constant heating rate experiments (logarithmic scale was used for y-axis).

Table 1. Change in flash sintering temperature at different electric-fields, at 20 mA/mm^2 for constant heating rate experiments

E.Field-Current Density (V/cm)-(mA/mm ²)	Power Dissipation (mW/mm ³)	Specimen Temperature (Calculated) (°C)	Flash Temperature (°C)
100-20	54	1127	1090
185-20	80	1120	1040
250-20	109	1096	990
500-20	135	1029	900

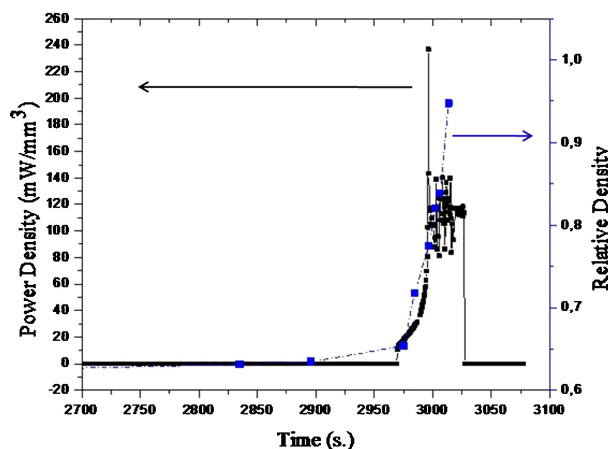


Fig. 5. Power density and relative density data of flash sintered sample at 250 V/cm , 20 mA/mm^2 .

densification. Power density is plotted on left y-axis and relative density is plotted with dotted curve referring to on the right y-axis. A rise in conductivity (power density) and rapid densification in the sample appeared to be simultaneous. Sample continued to shrink during current control region.

Linear shrinkage strain data of conventionally sintered and flash-sintered samples at different electric-fields are shown in Fig. 6. During flash sintering experiments the sample moved at the later stages of the measurement. Therefore, the full shrinkage range could not be measured/observed for flash sintered samples. Therefore, the last data point in the linear shrinkage curves did not correspond to the final shrinkage. For conventionally sintered sample (black curve) after 900°C a gradual decrease in length of

the sample was observed. For flash sintered samples a sharp shrinkage was observed starting at the power spike temperature. With increasing the field strength, flash temperature and the shrinkage temperature decreased. The highest linear shrinkage was observed at a field strength of 250 V/cm. Current localization was observed for a sample that was flash sintered at a very high field of 500 V/cm. (image not shown). This sample was not sintered homogeneously and the final density was rather low. While keeping the electric-field at 250 V/cm, when the current density was increased to 40 mA/mm², melting was observed in certain regions of the sample that were close to the platinum wires. At the low current density limit (7 mA/mm²), the current was not enough to spread the flash through the sample.

Density of the samples were measured by archimedes method and analyzed by UTHSCSA Image Analysis Program from polished surfaces of the samples shown in **Table 2**. For samples with low density, Archimedede's technique consistently gave lower densities due to incomplete wetting of open pore surfaces (i.e. for samples with densities lower than 95% of theoretical density).

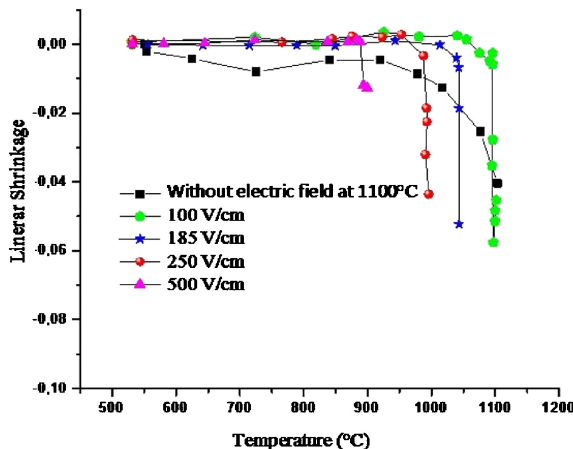


Fig. 6. Linear shrinkage strain for conventional and flash sintered samples at different electric-fields.

Table 2. Density of the samples flash sintered and conventional sintered

E.field-Current density-time	Density (Th.D) % (Archimedes)	Density (Th.D) % (Image Analysis)
100 V/cm-20 mA/mm ² -30 s.	79	89.8 ± 1.3
185 V/cm-20 mA/mm ² -30 s.	84	89.0 ± 1.3
250 V/cm-20 mA/mm ² -30 s.	94	94.6 ± 0.1
250 V/cm-20 mA/mm ² -60 s.		92.0 ± 0.8

The highest density ($94.6 \pm 0.1\%$ ThD) was obtained for the sample flash sintered at 250 V/cm-20 mA/mm² for 30 s. The density of the samples decreased for samples subjected to prolonged flash-sintering conditions. The de-densification tendency in KNN ceramics with longer sintering times could be seen in the samples flash-sintered for 60 s under 250 V/cm field strength and 20 mA/mm² current density. Grain growth was observed after 30 s. sintering duration (**Fig. 7**).

Chemical composition of flash sintered sample (250 V/cm electric-field, 20 mA/mm² for 30 s.) at micrometer level was investigated using an SEM (JEOL 6010 LV) equipped with an EDX detector. EDX mapping analysis, shown in **Fig. 8**, revealed while O and Nb distributions were homogenous, the distributions of Na and K were not. Regions rich in Na was depleted of K and vice versa. The EDX mapping revealed a core-shell type microstructure where K-rich regions seemed to constitute the shell around the Na-rich regions.

When a flash sintered sample was heat treated at 1000°C after 4 h the core-shell morphology has disappeared (**Fig. 9**). It was observed that 4 h of conventional heat treatment was enough to diffuse K ions into the core and Na ions outwards to shell to establish the equilibrium stoichiometry of KNN.

Densities of flash sintered for 30 s. and flash sintered + heat treated samples are 94 and 95.5%, respectively. Reduction in the pore size was observed with the heat treatment.

Table 3 shows the results of EDX chemical composition of Na, K and Nb. During the point analysis of different regions for quantification Na K α , K K α and Nb L α spectral lines were used. Na/K ratio in the shell is about 0.75 whereas it is 1.53 in the core. After the 4 h heat treatment Na/K ratio became 0.90. For quantification, k-correction factors listed in the manufacturer's tables were used.

For conventionally sintered sample Na and K distribution was homogenous. Na/K value was 0.90. Na value is slightly lower than K. In the literature Na₂O evaporation was given as the main cause of this discrepancy (**Fig. 10**). Another reason for this deviation from nominal Na/K ratio could be the difficulties in measuring Na/K ratio without an internal standard.²³⁾

The sample flash sintered at 250 V/cm electric-field, 20 mA/mm² for 30 s. was investigated with a scanning transmission electron microscope (STEM) to have a better understanding of this heterogeneous cation distribution. HRTEM image of the grain boundary in flash-sintered sample is shown in **Fig. 11**. The image was taken with the part of the boundary set at edge-on condition. Neither an amorphous layer nor second phase were observed within grain boundary.

Annular dark field scanning transmission electron microscope

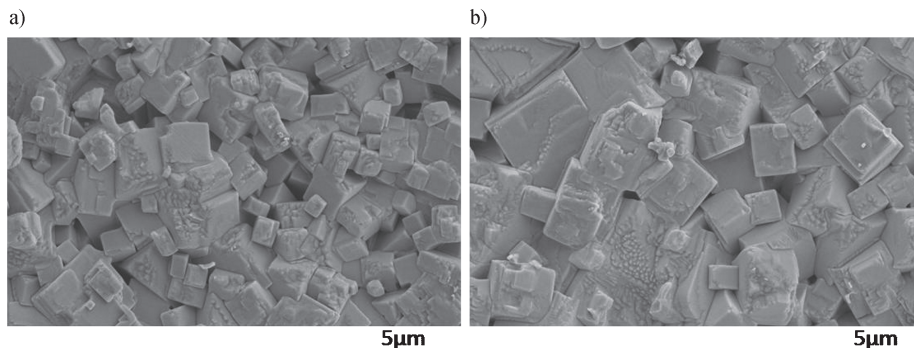


Fig. 7. SEM micrograph of flash sintered sample at 250 V/cm, 20 mA/mm² for a) 30 s. b) 60 s. (After 30 s of flash-sintering grain growth became obvious).

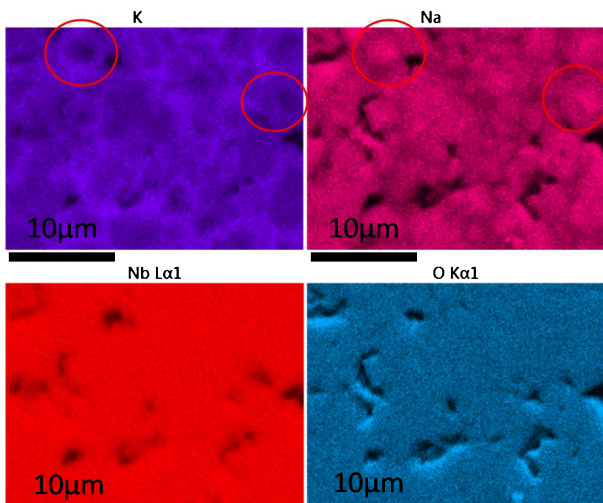


Fig. 8. Elemental mapping of Na, K, O, and Nb for flash sintered sample at 250 V/cm electric-field, 20 mA/mm² for 30 s. Circles indicate core-shell regions.

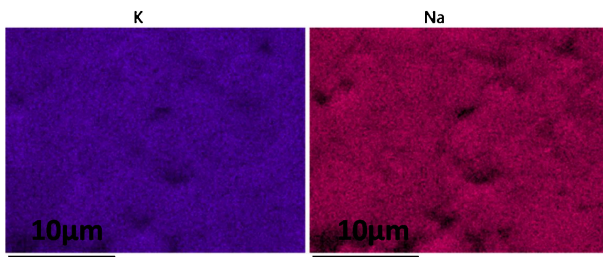


Fig. 9. Elemental mapping of Na and K for flash sintered and heat treated sample at 1000°C for 4 h.

Table 3. EDX Quantification values of flash sintered and flash sintered+heat treated sample

		Na	K	Na/K
Flash sintered	Shell-K rich region (% atomic)	42.7	57.3	0.75
	Core-Na rich region (% atomic)	60.5	39.5	1.53
Flash sintered+heat treated (%) atomic)		44.6	49.4	0.90

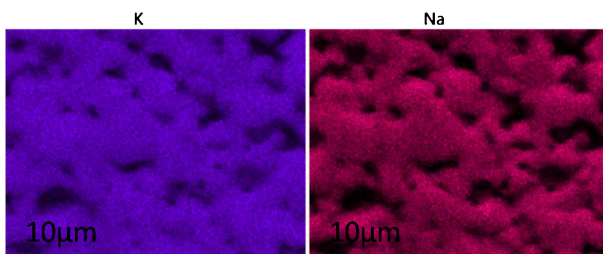


Fig. 10. Elemental mapping of Na and K for conventionally sintered sample at 1100°C for 2 h.

(ADF-STEM) image and the corresponding EDX elemental distribution maps for Na and K are shown in Fig. 12. The microstructure appears to be chemically heterogeneous in terms of sodium and potassium distribution. In the EDX map sodium-rich regions were presented with red color and potassium-rich regions were presented with green color. Therefore the orange color corre-

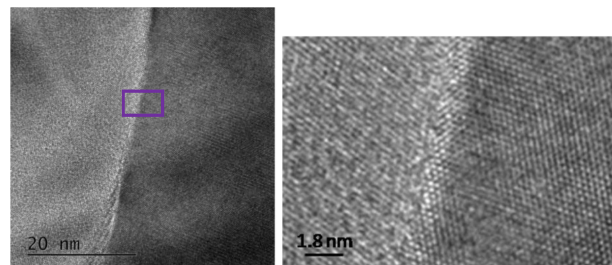


Fig. 11. HRTEM image of the grain boundary.

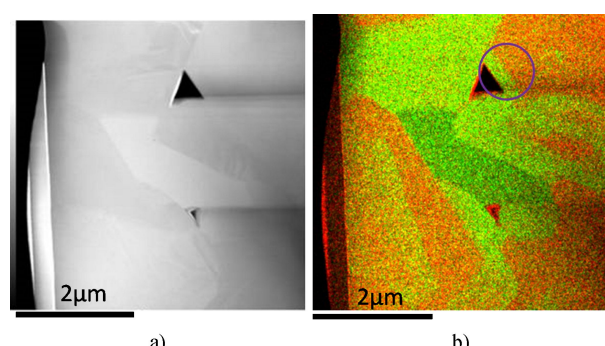


Fig. 12. a) STEM ADF image and STEM-EDX analysis a) STEM ADF image, b) STEM-EDX color maps: K and Na ion atom distribution (K: green, Na: red).

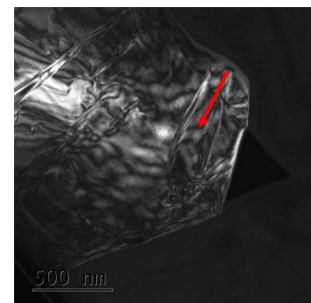


Fig. 13. Dark field TEM images of the region shown in Fig. 12(b) indicated with a circle. The two images are rotated with respect to each other. The triangular hole (dark in both images) is the reference feature.

sponded to sodium rich regions that also contained some amount of potassium. The predominantly green grain in the middle of the map appeared to be potassium niobate. The edges of triple point pockets appeared to be sodium covered. A closer examination of ADF-STEM image along with EDX maps revealed that the chemical heterogeneity was at the intra-grain level, i.e. a certain core-shell appearance was observed in some of the grains.

The region shown in the upper right corner of Fig. 12(b) (circled) was analyzed by dark field imaging (DF-TEM). This region was composed of only one grain. DF-TEM image of that region is shown in Fig. 13. It revealed that the chemical boundary was within a single grain. Inside this grain several defects could be observed. The chemical boundary was in between these defects (indicated with red arrow) and did not overlap with any visible defect (Fig. 13).

Chemical boundaries were not coinciding with structural boundaries as would be expected. From TEM dark field images and from diffraction analysis, the grain boundaries were deter-

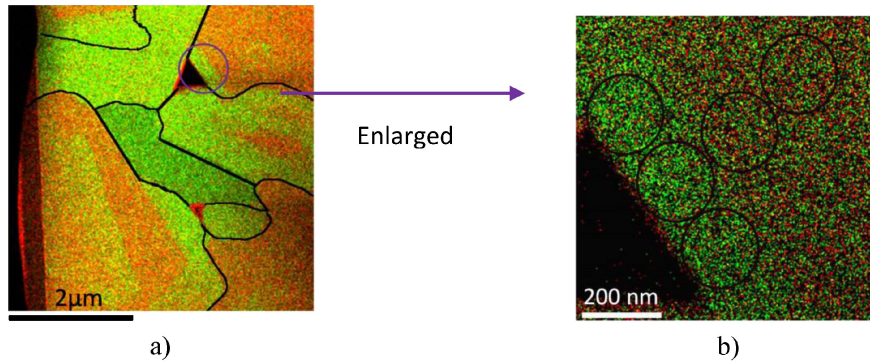


Fig. 14. STEM-EDX color maps showing analysis K and Na ion atom distribution (K: green, Na: red), a) Grain boundaries as determined from depending on diffraction analysis indexing, b) Enlarged view of the edge region encircled near the triple point pore.

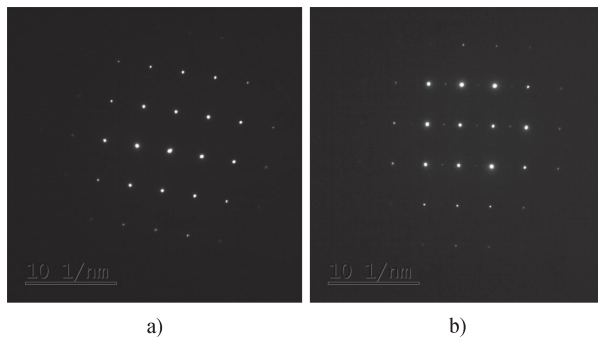


Fig. 15. Diffraction patterns of a) K rich region, b) Na rich region.

mined and overdrawn on to the EDX elemental map in **Fig. 14**. In the chemically heterogeneous region diffraction analyses were performed. Indexing of diffraction patterns were done by using FindIt and JEMS computer programs. Figure 14(a) shows how Na and K atoms were distributed between and within the grains.

Figure 14(b) shows the zoomed-in area that is indicated in Fig. 14(a) with a circle. Although the boundary between the two regions with different chemical compositions was roughly parallel to a crystallographic plane, the boundary was not atomically sharp, i.e. not bound by a single crystallographic plane. Diffraction analyses done in the two chemically different regions within the same grain revealed that the two regions are structurally not equal either. The diffraction patterns taken from the K-rich region showed, orthorhombic [120] zone axis pattern belonging to Bmm2 space group where [001] is present if l is even (or pseudo-cubic [112] zone axis) [**Fig. 15(a)**]. On the other hand, the diffraction patterns taken from Na-rich regions showed same zone axis with extra weak spots between the (002) strong spots (or pseudo-cubic [112] zone axis with weak spots between the (110) strong spots) [**Fig. 15(b)**].

Further crystallographic studies are underway to determine the structural modification that will give rise to such superlattice spots. At the moment it should suffice to say that they may be indicative of an ordering in [001] direction. It appears that the unit cell in this direction may be doubling in size. One possible reason for this could be a cation ordering giving rise to the diffraction pattern as shown in Fig. 15(b). Another explanation was given by Woodward and Reaney as alternation of octahedra tilt in consecutive unit cells.²⁴⁾ Two more grains with chemical K–Na zoning were studied and similar structural modification was observed.

In the literature Zhang S. and co-workers²⁵⁾ investigated $K_{0.5}$

Table 4. Flash sintering temperatures and corresponding applied fields for materials

Materials	Flash Temperature (°C)	Applied Electric-Field (V/cm)	References
ZnO-single crystal	870	300	22
ZnO powder	553	44	22
0.5 mol Bi_2O_3+ZnO	620	21	22
$SrTiO_3$	900	500	17
Co_2MnO_4	400	7.5	15
Mg doped Al_2O_3	900	>1000	14
TiO_2	800	250	18
$8Y_2O_3-ZrO_2$	900	~100	13
KNN	990	250	this study

$Na_{0.5}NbO_3$ ceramic by TEM. They observed two different regions along [112] zone axis. One of them contained strip-like domains. The other region was without domain contrast (featureless-domain). They claimed that depending on the KN–NN phase diagram, room-temperature $K_{0.5}Na_{0.5}NbO_3$ is a mixture of two phases without oxygen octahedral tilt: the K-rich Amm2 ($a^0a^0c^0$) phase and the Na-rich Pm ($a^0b^0c^0$) phase. They found a correlation between striplike domain and higher K content by EDX measurements. Certainly, further studies are necessary to bring a better explanation to the structural modifications happening to KNN during flash-sintering.

4. Discussion

After the flash sintering a strong tendency for facetting was observed under all sintering conditions (Fig. 7). Cube-like grains with large number of surface steps parallel to dominant crystallographic planes comprise the microstructure. Such steps are possibly reminiscent of strong faceted grain growth during flash sintering.²⁶⁾ Highest density, 94% Th.D., was observed for 30 s. sintering duration. Rapid grain growth started after 30 s. of sintering. This rapid grain growth coupled with strong facetting may be the reason for a reduction in density after 30 s. Although facetting was observed in the conventionally sintered samples it was not as dominant as it was in flash-sintered ones.

Table 4 shows flash sintering temperatures and corresponding applied fields for other materials. Although flash sintering is applicable to a different range of materials (ionic or electronic conductors or even to dielectric materials), (flash) sintering temperature and corresponding applied field are material dependent. For a mixed conductor like $CoMnO_4$, flash sintering was achieved at 7.5 V/cm and 400°C, whereas for the insulator Mg doped Al_2O_3

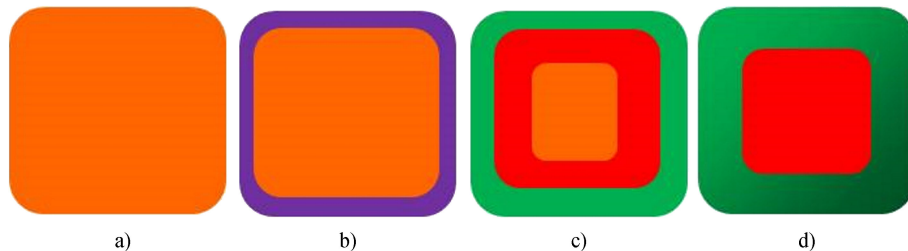


Fig. 16. Schematic of core–shell formation a) original composition $K_{0.5}Na_{0.5}NbO_3$, b) liquid formation, c) solidification of liquid with new composition, d) rearrangement of the solid composition).

higher than 1000 V/cm was necessary at 900°C to achieve a flash. As the conductivity (both ionic and electronic) of the “insulator” is increasing, both the electric-field and temperature required for flash-sintering tends to decrease.²²⁾ KNN being a piezoelectric insulator ceramic with negligible electronic conductivity behaves more similar to alumina than $CoMnO_4$ in flash sintering.

KNN samples flash sintered in this study revealed a core–shell structure and intra-granular variation in Na and K concentrations. There could be several origins for the existence of the observed “chemical” core–shell structure. One reason may be incomplete reactions during powder synthesis. The different decomposition temperatures of potassium and sodium carbonates could have caused heterogeneity in the KNN powders. However, powders used in these experiments were examined using SEM for core–shell structure before compacting. The powders did not show any chemical core–shell morphology. Another reason of this core–shell structure may be local melting starting at the grain boundaries due to joule heating. During the flash, the joule heating might have raised the temperature near the grain boundaries above the solidus temperature. This would create a K-rich liquid at the boundaries according to the equilibrium phase diagram between $KNbO_3$ and $NaNbO_3$.^{3),27)} During the flash because of local heating, the compositions of the melt and the neighboring core will change due to inter-diffusion between liquid shell and the solid core. During cooling liquid phase would recrystallize with a compositional gradation.

After flash sintering the Na/K+Na ratio of the core region was measured as ~60.5% with the help of EDS system attached to a SEM. The same ratio was ~43% in the shell.

KNN is a complete binary solid solution between $KNbO_3$ ($T_m \sim 1090^\circ C$) and $NaNbO_3$ ($T_m \sim 1420^\circ C$).³⁾ Small temperature changes below and above the solidus would create large compositional variations in the liquid and the solid. The KNN composition used in this study was 50% $KNbO_3$ /50% $NaNbO_3$. However, the composition of the shell was measured as 57% $KNbO_3$ and 43% $NaNbO_3$. The composition of the core was nominally 40% $KNbO_3$ and 60% $NaNbO_3$. Assuming that the compositional variations during cooling would be slower in the solid phase, i.e. in the core region, one can estimate the most likely temperatures that the boundaries in the polycrystalline ceramic could have reached during the flash. The 40:60 $KNbO_3$: $NaNbO_3$ solid composition would correspond to 1150°C for a 50:50 starting composition. This 40:60 $KNbO_3$: $NaNbO_3$ solid composition would be in equilibrium with a 78:22 $KNbO_3$: $NaNbO_3$ liquid composition as predicted in the phase diagram. The $KNbO_3$ -level in the re-crystallized shell region of the sample was lower than expected. It was observed that some of the excess K was accommodated in the $KNbO_3$ grains that formed in the microstructure as shown in Fig. 12(b). Some of the K_2O may have evaporated during the flash.

A model for the systematic of core–shell formation was

explained in Fig. 16 and in the following text;

The starting composition was 50% $NaNbO_3$ –50% $KNbO_3$ (a). During the flash grain boundary melting occurs and renders the liquid composition rich in potassium (b). After the flash during cooling (c) a K-rich shell and Na-rich core appear with maybe a small amount of original composition in the very center of the original grain. During the further sintering this small original composition may also be adjusted as shown in (d).

Different levels of homogeneity in the particle chemistry were possible due to different particle sizes and corresponding diffusion distances during the chemical variation in sintering.

Most of the studies on the subject claim there is a link between core–shell formation and liquid phase during sintering not only in KNN ceramics but also in other ceramic materials like $BaTiO_3$. Core–shell structure was observed for $(1-x)Na_{0.5}K_{0.5}NbO_3-xLiTaO_3$, modified with $BiScO_3$, $x = 0.5$ composition.²⁸⁾ In this study core–shell segregation was explained with an absence of a liquid phase during sintering. Addition of liquid-phase forming excess alkali metal oxides prevented core–shell appearance. It was suggested that producing a transient liquid phase promoted inter-diffusion and improved chemical homogeneity. Zhang and co-workers²⁵⁾ investigated cooling effect on the microstructure of KNN samples sintered in the solid+liquid region (sintered at 1170–1200°C) of the phase diagram for $x = 0.5$ composition. Na and K inhomogeneity was mostly reported in quenched samples. In those samples, they obtained disproportionation of alkalis into (i) K poor region, (25% K/K+Na), with an excess K-rich liquid film (57% K/K+Na) in the boundary and (ii) K richer regions (K/K+Na 37–44%). For furnace cooled or slow cooled samples, chemical heterogeneity was observed in different regions of the samples with K/K+Na ratios between 44 to 24%. They concluded that slow cooling let system to establish a more homogenous distribution of Na and K.

The formation of core–shell type chemical segregation during sintering was studied with different dopants in $BaTiO_3$ ceramics. Two mechanisms were proposed: First one explains the shell formation by solid-state diffusion of dopants into $BaTiO_3$ particles. Second one explains the shell formation by dissolution/precipitation of dopant from a liquid.²⁹⁾

Seon S.-C and co workers worked with bi-layer samples with different chemical compositions [94BaTiO₃–2Y₂O₃–2MgO–2SiO₂ (mol %) and 98BaTiO₃–2SiO₂ (mol %)] and grain sizes. They found a close crystallographic relationship between the core and the shell which was interpreted as an indication of an epitaxial grown layer by dissolution of small grains and precipitation of the dissolved material onto the growing grains. The electron-diffraction patterns from the core and the shell region showed that they have the same crystallographic orientation and the coherent interface between the core and the shell observed by HRTEM (High-Resolution TEM) confirming epitactic relationship.²⁸⁾

Randall et al. suggested that³⁰⁾ formation of liquid phase is a

prerequisite for the formation of core–shell structure. In addition, they suggest other prerequisites such as: solubility of $BaTiO_3$ into the glass, reprecipitation of $BaTiO_3$ including additives in perovskite structure, limited grain-growth process and limited interdiffusion such that a homogeneous distribution of dopants would be retarded. The process was explained as follows: for $BaTiO_3$ system when the saturation level of liquid phase was established in terms of $BaTiO_3$, solution-precipitation proceeded by dissolution of smaller grains and growing of larger ones. As the process continued, concentration of the additives in the solid increased whereas it was depleted in the liquid. They claimed that the concentration difference between the core and shell created a driving force for diffusion. Since the core–shell morphology was a thermodynamically unstable structure, high sintering temperatures and/or long sintering times provided a more homogeneous distribution and eliminated the core–shell. Lu et al. reported homogenization in the $BaTiO_3$ – ZrO_2 system with up to 60 h of sintering.³¹⁾ Chemical homogenization was also shown in this study when the flash-sintered core–shell structures were annealed at high temperatures.

In this study EDX quantification of core–shell morphology indicated that a liquid grain boundary region formed during flash. A rise in the temperature caused by Joule heating during flash brought the system into the two-phase region in the phase diagram. In this two-phase region grain boundaries were liquid and rich in potassium whereas neighboring core was solid and deficient in potassium. The liquid at the boundaries increased conductivity (stronger Joule-heating) and the sintering rate. Compositional variation persisted during cooling thereby creating a core–shell microstructure.

5. Conclusions

When KNN polycrystalline compacts were flash sintered at 990°C in 30 s 94% of theoretical density was obtained. Similar densities can only be obtained at 1100°C and after 2 h of conventional sintering. Core–shell like chemical disproportionation was observed by SEM-EDX studies where the shell was rich in K and the inner layers were rich in Na. Joule-heating driven selective grain boundary melting which was one of the proposed mechanisms to explain flash sintering in the literature, appears to be the reason of this core–shell like structure. EDX quantification showed that Na/K+Na ratio in the shell was on the average 43% whereas in the core it was around 60.5%. The coexistence of these compositions in the (molten/re-crystallized) shell and in the (solid) core regions would correspond to an effective temperature of ~1150°C in the existing $KNbO_3$ – $NaNbO_3$ binary phase diagram. This temperature is in the liquid+solid two phase region for a starting composition of 50:50 $KNbO_3$ and $NaNbO_3$. During the flash and consequent cooling diffusion between the shell and the core created a compositional variation. A heat treatment homogenized the Na/K ratio at 0.90 closer to the nominal value of 1.0. Additional diffusion during heat treatment let the system come to an equilibrium chemical composition with a more homogenous Na and K distribution. STEM-EDX analysis showed that this variation of Na and K was in an intra-grain level and it appeared to have led to a ordering (cation or octahedral tilt) along 002 direction in the Na rich core.

Acknowledgement This work was supported by the Scientific and Technological Research Council of Turkey (TUBITAK) with 2214/A Program under Grant 1059B141300914.

This research used resources of the Center for Functional Nano-

materials, which is a U.S. DOE Office of Science Facility, at Brookhaven National Laboratory under Contract No. DE-SC0012704.

References

- J. Rödel, W. Jo, K. T. P. Seifert, E. M Anton and T. Granzow, *J. Am. Ceram. Soc.*, **92**, 1153–1177 (2009).
- K. Wang and J.-F. Li, *Advanced Ceramics*, **1**, 24–37 (2012).
- E. Ringgaard and T. Wurlitzer, *J. Eur. Ceram. Soc.*, **25**, 2701–2706 (2005).
- S. Zhang, R. Xia and T. R. Shrout, *J. Electroceram.*, **19**, 251–257 (2007).
- C. Sen, B. Alkan, I. Akin, O. Yucel, F. C. Sahin and G. Goller, *J. Ceram. Soc. Japan*, **119**, 355–361 (2011).
- E. Mensur Alkoy and M. Papila, *Ceram. Int.*, **36**, 1921–1927 (2010).
- E. Hollenstein, M. Davis, D. Damjanovic and Nava Setter, *Applied Physics Letters*, **87**, 182905 (2005).
- M. Matsubara, T. Yamaguchi, K. Kikuta and S.-I. Hirano, *Jpn. J. Appl. Phys.*, **44**, 6136–6142 (2005).
- Y. Saito, H. Takao, T. Tani, T. Nonoyama, K. Takatori, T. Homma, T. Nagaya and M. Nakamura, *Nature*, **432**, 84–87 (2004).
- M. Cologna, B. Rashkova and R. Raj, *J. Am. Ceram. Soc.*, **93**, 3556–3559 (2010).
- R. Raj, M. Cologna and J. S. C. Francis, *J. Am. Ceram. Soc.*, **94**, 1941–1965 (2011).
- R. Raj, *J. Eur. Ceram. Soc.*, **32**, 2293–2301 (2012).
- H. Yoshida, Y. Sakka, T. Yamamoto, J.-M. Lebrun and R. Raj, *J. Eur. Ceram. Soc.*, **34**, 991–1000 (2014).
- M. Cologna, J. S. C. Francis and R. Raj, *J. Eur. Ceram. Soc.*, **31**, 2827–2837 (2011).
- A. L. G. Prette, M. Cologna, V. Sglavo and R. Raj, *J. Power Sources*, **196**, 2061–2065 (2011).
- E. Zapata-Solvas, S. Bonilla, P. R. Wilshaw and R. I. Todd, *J. Eur. Ceram. Soc.*, Short communication **33**, 2811–2816 (2013).
- A. Karakuscu, M. Cologna, D. Yarotski, J. Won, J. S. C. Francis, R. Raj and B. P. Uberuaga, *J. Am. Ceram. Soc.*, **95**, 2531–2536 (2012).
- S. K. Jha and R. Raj, *J. Am. Ceram. Soc.*, **97**, 527–553 (2014).
- J.-W. Jeong, J.-H. Han and D.-Y. Kim, *J. Am. Ceram. Soc.*, **83**, 915–918 (2000).
- V. Ravikumar, R. P. Rodrigues and V. P. Dravid, *J. Am. Ceram. Soc.*, **80**, 1131–1138 (1997).
- J. Narayan, *Scr. Mater.*, **69**, 107–111 (2013).
- Y. Zhang, J.-I. Jung and J. Luo, *Acta Mater.*, **94**, 87–100 (2015).
- S. Sturm, A. Bencan, M. A. Gulgul, B. Malic and M. Kosec, *J. Am. Ceram. Soc.*, **94**, 2633–2639 (2011).
- D. I. Woodward and I. M. Reaney, *Acta Crystallogr., Sect. B: Struct. Sci.*, **61**, 387–399 (2005).
- S. Zhang, H. J. Lee, C. Ma and X. Tan, *J. Am. Ceram. Soc.*, **94**, 3659–3665 (2011).
- S.-J. L. Kang, Sintering Densification Grain Growth Microstructure Elsevier (2005).
- B. Jaffe, H. Jaffe and W. R. Cook, “Piezoelectric ceramics”, Academic Press, London (1971).
- F. Zhu, M. I. B. Ward, J.-F. Li and S. J. Milne, *Acta Mater.*, **90**, 204–212 (2015).
- S.-C. Jeon, C.-S. Lee and S.-J. L. Kang, *J. Am. Ceram. Soc.*, **95**, 2435–2438 (2012).
- C. A. Randall, S. F. Wang, D. Laubscher, J. P. Dougherty and W. Huebner, *J. Mater. Res.*, **8**, 871–879 (1993).
- H. Y. Lu, I. S. Bow and W. H. Deng, *J. Am. Ceram. Soc.*, **73**, 3562–3568 (1990).